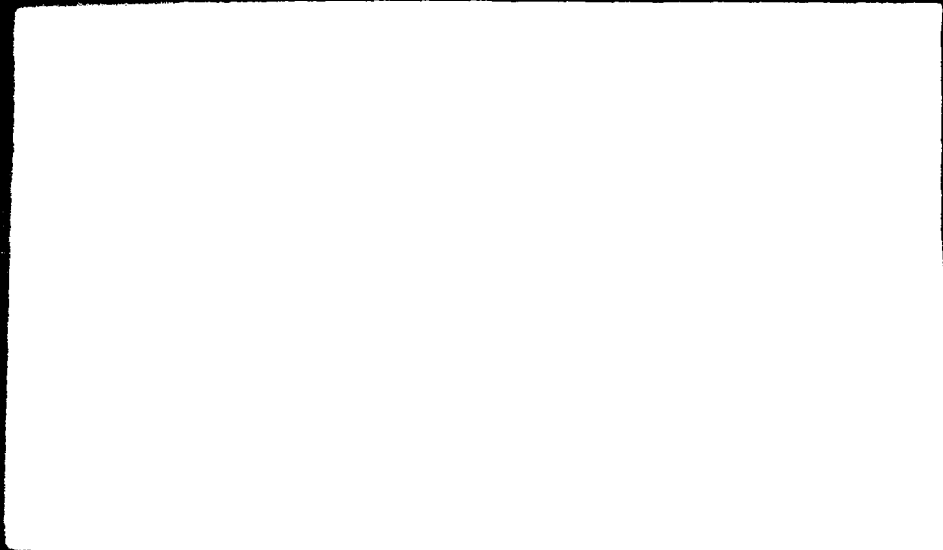


ADA 032450

ONE COPY ONLY  
of complete text to TR041-761  
7

①



D E C  
NOV 23 1978  
C

DISTRIBUTION STATEMENT A  
Approved for public release;  
Distribution Unlimited

REPORT DOCUMENTATION PAGE		READ INSTRUCTIONS BEFORE COMPLETING FORM
1. REPORT NUMBER TR071-761 ✓	2. GOVT ACCESSION NO.	3. RECIPIENT'S CATALOG NUMBER
4. TITLE (and Subtitle) Design and Evaluation of a Balloon-Borne Electric Field Sensor		5. TYPE OF REPORT & PERIOD COVERED Technical ✓
		6. PERFORMING ORG. REPORT NUMBER
7. AUTHOR(s) Hugh Joseph Christian, Jr		8. CONTRACT OR GRANT NUMBER(s) N00014-75-C-0139 ✓
9. PERFORMING ORGANIZATION NAME AND ADDRESS Rice University - A. A. Few ✓ Post Office Box 1892 Houston, Texas 77001		10. PROGRAM ELEMENT, PROJECT, TASK AREA & WORK UNIT NUMBERS NR211-191
11. CONTROLLING OFFICE NAME AND ADDRESS Atmospheric Sciences Program Code 465 Office of Naval Research Arlington, Virginia 22217		12. REPORT DATE 18 October 1976
		13. NUMBER OF PAGES 5 (complete text 78 pp)
14. MONITORING AGENCY NAME & ADDRESS (if different from Controlling Office)		15. SECURITY CLASS. (of this report)
		15a. DECLASSIFICATION/DOWNGRADING SCHEDULE
16. DISTRIBUTION STATEMENT (of this Report) Approved for public release; distribution unlimited.		
17. DISTRIBUTION STATEMENT (of the abstract entered in Block 20, if different from Report)		
18. SUPPLEMENTARY NOTES M.S. thesis published at Rice Univ. May 1976. Copies of text available from National Technical Information Service, Springfield, VA 22151. This is standard distribution in accord- ance with contract.		
19. KEY WORDS (Continue on reverse side if necessary and identify by block number) Balloon Instrumentation, Electric Field Sensors, Atmospheric Electric Fields, Thunderstorm Electricity		
20. ABSTRACT (Continue on reverse side if necessary and identify by block number) A new instrument is described for the measurement of electric fields. This application uses a spherical superpressure balloon with an exterior conductive coating and the instrument package located inside the balloon as the lifting device, the sensor, and the instrument shield. This unique design offers superior performance and opportunities here-to-fore inaccessible. ↑		

1

9 Master's thesis,

RICE UNIVERSITY

6 DESIGN AND EVALUATION OF A BALLOON-BORNE  
ELECTRIC FIELD SENSOR.

10 by Joseph  
Hugh // Christian, Jr

11 18 Oct 76

A THESIS SUBMITTED  
IN PARTIAL FULFILLMENT OF THE  
REQUIREMENTS FOR THE DEGREE OF

12 83p.

MASTER OF SCIENCE

14 TR 71-761

Thesis Director's Signature:

*Antonia F...*

Houston, Texas

September, 1975

15 N 14-75-C-139

D.D.S.  
RECEIVED  
NOV 23 1975  
C

DISTRIBUTION STATEMENT A  
Approved for public release;  
Distribution Unlimited

1473  
408 798  
43

DESIGN AND EVALUATION OF A BALLOON-BORNE  
ELECTRIC FIELD SENSOR

by

Hugh J. Christian, Jr.

ABSTRACT

A balloon-borne instrument has been developed which has the capability of making absolute measurements of the vector electric field inside thunderstorms and under fair weather conditions. Known as the Balloon Electric Field Sensor (BEFS), this device consists of a super-pressure spherical balloon and the associated electronics package which is mounted inside the balloon. The balloon, which has its surface divided into four conducting regions (in the shape of lunes), serves as both the measuring platform and the sensing element. Because of spherical symmetry and the absence of protrusions, calibration procedures are simplified, unknown field distortion factors are eliminated and corona problems are minimized.

The BEFS measures the vertical and horizontal components of the ambient field in a total of three modes. By correlating these modes it is possible to separate the true field from various distorting effects.

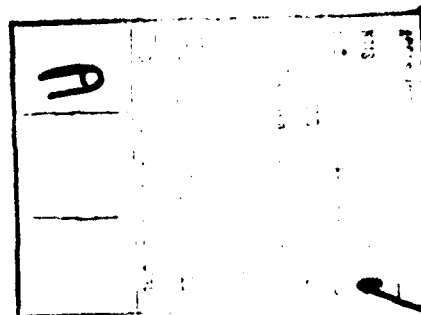


## TABLE OF CONTENTS

	Page
CHAPTER 1 INTRODUCTION	1
CHAPTER 2 HISTORY OF CLOUD ELECTRIC FIELD MEASUREMENTS	3
2.1 Measurement Vehicles	3
2.2 Detector Types	6
2.3 Previous Measurements	8
CHAPTER 3 A NEWLY DESIGNED ELECTRIC FIELD SENSOR	11
3.1 Introduction	11
3.2 Physical Description	12
3.3 Theory of Operation	14
3.4 Modes of Operation	17
3.5 Electronics Package	18
3.6 Design Advantages	20
3.7 Design Limitations	21
3.8 External Error Sources	22
CHAPTER 4 TEST FLIGHT	28
4.1 Initial Flight	28
4.2 Problem Areas	29
4.3 Data Analysis	31
4.3.1 Low-Pass Filter	31
4.3.2 Differentiating the Orientation Data	32
4.3.3 Integrating the Electric Field Data	37

	Page
CHAPTER 5 THE NEXT FLIGHT	41
5.1 Instrument Modifications	41
5.2 Flight Objectives	43
ACKNOWLEDGEMENTS	45
APPENDIX A ELECTRICAL PROPERTIES OF A CONDUCTING SPHERE	
A.1 Conducting Sphere in an Electric Field	A1
A.2 Total Induced Charge on a Lune	A7
A.3 Total Induced Charge vs Orientation	A8
APPENDIX B ELECTRONICS PACKAGE	
B.1 Electrometer Amplifier	B1
B.2 Charge Amplifier	B1
B.3 Compressor Amplifier	B2
B.4 Auxiliary Data Circuits	B2
B.5 Digital Control Board	B2
B.6 Digital Conversion Board	B2
B.7 Transmitter Board	B3
REFERENCES	
FIGURE CAPTIONS	
FIGURES	

## CHAPTER I

### Introduction

The electrical nature of the thunderstorm remains a mystery despite years of research by numerous investigators. The mystery persists because of the difficulties involved in measuring and modeling the storm. Thunderstorms are dynamic in time and space. A single cell may typically pass through its life cycle consisting of cumulus, mature, and dissipating stages, in less than an hour. A single storm may be composed of a number of cells, each at a different phase. Add to this complexity the violence inherent in many storms, and it is not surprising that much of the physics remains clouded.

It is generally accepted that the outstanding questions to be answered on the electrical properties of the thunderstorm are:

- 1) What is the Charge Generation Mechanism? That is, how do cloud particles become charged and what particles become charged?
- 2) What is the Charge Separation Mechanism? Once generated, what forces drive net charge to different regions of the cloud?

The instrument described in this thesis was developed in order to provide data which would help in the answering of these questions. The Balloon Electric Field Sensor, or BEFS, was designed to measure a full profile of the vector electric field, from the ground through the

top of a cloud. These measurements should provide, for the first time, information on the total magnitude of the field, the relative location of principal charge centers, the difference between ground and cloud measurements, and a full profile of the field as a function of height. Improved information on these parameters should help one choose between the many charge generation and separation models.

While the BEFS was primarily designed to measure foul weather electric fields, it is also capable of measuring the fair weather electric field. The fair weather field is thought to be produced by the world-wide random thunderstorms which maintain a potential difference between the ionosphere and the earth's surface. The fair weather field is typically four orders of magnitude smaller than the foul weather field.

While the fair weather field is far better understood than the foul weather field, there remain many outstanding questions, such as:

- 1) How large and systematic are the diurnal and seasonal changes? What causes them?
- 2) How do the electric field and the other atmospheric electrical properties change with height?
- 3) How strongly are fields mapped between the ground and the ionosphere?

Because of its ability to make accurate profile measurements, the BEFS could supply unique information toward answering these questions. The only modification necessary in order to measure either of these fields is to change the sensitivity of the front end electrometer.

## CHAPTER II

### History of Cloud Electric Field Measurements

#### 2.1 Measurement Vehicles

Since the day of Benjamin Franklin, scientists have attempted to make in-situ measurements of the electrical properties of thunderstorms. None of the attempts to date have been as fundamentally successful as Dr. Franklin's, although most are now far safer. Almost all of today's information on the electrical properties of thunderstorms comes from ground-based remote sensing techniques. Yet it is imperative that in-cloud measurements be made since conductivity differences between cloud and clear air, and perturbing effects due to the conducting and ion producing earth may often cause the electrical parameters measured at the earth's surface to be radically different than the actual phenomenon occurring within the cloud. In-cloud measurements have been notably uninformative, although a number of newly developed instruments may change this situation.

There have been a number of different platforms used in the measurement of thunderstorm electric fields. The use of rockets, airplanes, dropsondes, and teathered and free balloons have all been attempted, rejected, and resurrected. Each platform inserts a compromise into the measurement being attempted. Each platform maintains a relative advantage for certain measurements.

The airplane, independently of how it is instrumented, is a useful, though complex platform. With an airplane one can fly to virtually any region of a cloud and make measurements over the age of the storm. It is the only instrument that can be used to measure horizontal cross-sections of the cloud.

Despite these advantages, the airplane presents some obvious limitations. The airplane is a large, irregularly-shaped conductor. It strongly distorts the ambient electric field; the magnitude of this distortion is difficult to determine. In practice the airplane's "enhancement factor" is calibrated by flying the aircraft near the Earth's surface in clear weather, and comparing the aircraft measurements with measurements made on the ground. The inaccuracies in this procedure arise from the fact that:

- (a) The electric field at the height of the aircraft is not well known;
- (b) It is assumed that the presence of the conductive earth does not alter the aircraft field distortion, and
- (c) This procedure does not determine the enhancement factor as a function of the aircraft orientation.

Other disadvantages of an aircraft facility are that it is expensive to operate and maintain, there is a true hazard to aircraft and personnel when flying through the center of active thunderstorms, vertical cross-sections cannot easily be measured, and the very strong enhancement factors at the tips of the aircraft may cause corona discharge currents

to be produced. Corona currents effectively distort the electric field that the aircraft instruments sense and prevent the stronger fields from being accurately measured.

Small rockets have been flown through thunderstorms with a degree of success (Winn and Moore, 1972). These rockets were small enough to calibrate in the laboratory and were relatively inexpensive. A major disadvantage lies in their flight duration of only one minute. A large number of launches would be necessary to obtain any information on storm dynamics. In addition rockets in general seem to be susceptible to the same corona problems as aircraft, and to date, only the field component perpendicular to the rocket trajectory has been measured.

Dropsondes have been used to measure electric fields in thunderstorms (Evans, 1969). The biggest liabilities arise from their reliance on aircraft to drop them over a cloud top. This results in logistic, time, and expense problems which, to date, have limited their use. Other problems which may typically be associated with dropsondes are errors due to differential motion between the sonde and the drag chute, and, as always, corona discharge.

Balloons were the vehicles used by Simpson and Robinson (1940) during a series of flights which even today provide some of the best available data of in-situ thunderstorm electric field measurements.

Balloons, in general, make desirable platforms for a number of reasons:

- a) They are slow moving and can directly sense the growth and collapse of electric fields. A balloon can thus make measurements on the temporal history of a storm.

- b) The balloon is virtually in harmony with its environment. Its only motion relative to the storm is its vertical rise. This slow relative motion tends to reduce static charge build-up.
- c) Since the balloon is launched from the ground through the cloud top, the electric field as a function of height could theoretically be measured (if a properly designed detector is used).

Naturally there exist limitations associated with the use of balloon-borne detectors. The two biggest problems are associated with the lack of control over the balloon. Once the balloon is launched, one has no control over where it will go. Also, one must wait for a storm to pass overhead before a launch can be attempted. This actually is a small handicap since all inter-cloud measurements should be correlated with ground based data.

Problems such as field distortion and corona discharge are not limitations inherent in the use of a balloon borne instrument. They are strictly a consequence of detector design.

## 2.2 Detector Types

There have been as wide a variety of detectors designed for in-cloud measurements of electric fields as there have been means for lifting these detectors into the cloud. This ensemble of detectors tends to divide into three major types: 1) corona current detectors,

2) high impedance potential probes, and 3) electric field mills.

Corona current detectors as flown by Simpson and Scarse (1937), Simpson and Robinson (1940), and Chapman (1943) measure the corona current flowing through two long vertical wires pointed in opposite directions in the ambient electric field. With this design one can deduce the sign of the vertical component of the electric field, but can only get a rough estimate of the magnitude of this field component because of the non-linear relationship between corona current, vector field strength, cloud conditions, and altitude.

The use of high impedance potential probes has generally been restricted to ground based installations, although Masterson (1974) has installed them aboard aircraft. The potential probe makes a direct measurement of the potential difference between two conductors by maintaining a very high impedance between these conductors. If this impedance is much larger than the impedance of the air between the probes, then each conductor should reach the potential of the average atmospheric potential surrounding the probes.

These probes probably are of limited use in a thunderstorm because the conductivity in a cloud is thought to be much smaller than the fair air conductivity (Wilson, 1956). When the air conductivity becomes too small, the potential probe loses accuracy. Any high impedance instrument of this type is also very susceptible to damage from the before-mentioned corona discharge currents.

A popular modification to the potential probe is the addition of the radioactive equalizer. This equalizer ionizes the air in the immediate vicinity of the probe and thus lowers the time constant

between the air and the probe. This impedance matcher reduces the amount of impedance that must be maintained between the probes, but the requirements are still very stringent in the cloud environment.

A third detector type is the widely used field mill. The standard field mill measures the charge induced on an insulated plate whose exposure to the external electric field is modulated by a motor driven system of conducting shields.

Various versions of the electric field mill have been adapted to take in cloud measurements from airplanes (Kasemir, 1972), rockets (Winn and Moore, 1971) and (Winn, et al., 1974), tethered balloons (Rusk and Moore, 1974), and free balloons (Christian and Few, 1974) and (Winn and Byerly, 1975). Unlike the previously discussed detectors, there is no inherent limitation on one's ability to measure atmospheric electric fields with a field mill. Limitations exist only in the quality of the detector design and its integration with the lifting platform.

### 2.3 Previous Measurements

The first useful measurements of electric fields inside thunderstorms were made by Simpson and Scarse (1937) and Simpson and Robinson (1940). Although they received little information on the magnitude of the field, they were able to measure the field sign. With over thirty sondes launched through thunderstorms, they were able to deduce information on the possible location and sign of charge centers. On the average, they found a region of negative charge centered just above the

-5°C isotherm and a region of positive charge centered just above the -20°C level. They usually found small regions of positive charge located in the lower levels of the cloud.

A series of sixty-one rocket launches by Winn, Schwede, and Moore (1974) made short time measurements of the horizontal electric field. They found that very intense horizontal fields ( $4 \times 10^5$  v/m) do exist in thunderstorms and that these fields tend to be associated with the melting layer. They measured horizontal fields with magnitudes greater than  $10^5$  v/m less than 10% of the time and concluded that the regions of very intense fields and high charge concentrations must be confined to relatively small volumes.

In an even more recent experiment, Winn and Byerly (1975) launched a number of balloon borne field meters into thunder clouds. Like the rocket experiment, these instruments could measure only the horizontal component of the electric field. Because Winn had no information on the location of the balloon with respect to the storm, he did not attempt to determine a vertical profile of the horizontal electric field. He analyzed that portion of his data that contained information on lightning produced horizontal field changes. (He has recently modified this instrument to measure the full vector field.)

From looking at two figures he included with his paper, it appears that the magnitude of the horizontal field starts to intensify around the 0°C level. It must be reiterated that this is speculative because there was no real knowledge of either the altitude or horizontal position of the balloons during their flights.

In a series of flights using cylindrical field mills mounted on aircraft, Holitzer et al. (1974) measured the vertical component of the electric field inside thunderclouds. Their averaged results seem to indicate that a typical mid-western storm contains a net negatively charged region around the  $-5^{\circ}\text{C}$  level, a positively charged region at the  $-15^{\circ}\text{C}$  level, and an additional net positive region near the  $+5^{\circ}\text{C}$  isotherm.

The four experiments that were just discussed probably represent the best information on in-cloud electric fields available today, yet none of them measured both the vertical and horizontal fields simultaneously. Only two of them were compared with ground based data.

If one were bold enough, he could lace the information from these four experiments together and come up with some sort of idealized electric field structure. This procedure would be very suspect because of the different types of storms each of these instruments was flown in, because of the strikingly different way in which each of these instruments made the measurements, and because of the obvious limitations of each of these experiments. It is obvious that a single instrument must make vector measurements of the electric field before storm field structure can be delineated. These measurements must be made with knowledge of the sensor's location in time and space and with respect to the storm's development.

## CHAPTER III

### A Newly Designed Electric Field Sensor

#### 3.1 Introduction

The goal of this project was to design a balloon-borne detector that could accurately measure the total vector electric field, both inside a thunderstorm and under fair weather conditions. In order to achieve this goal it was necessary to minimize the inherent problems encountered by many of the earlier instruments.

As described in Chapter 2, there have been two classic methods used in measuring atmospheric electric fields. The two approaches may be classified under A.C. and D.C. coupled instruments. With a D.C. instrument such as a high impedance probe, one determines the field intensity by measuring the potential difference between conducting probes which are a known distance apart. While this is a simple approach, it has significant limitations.

At sea level, atmospheric conductivity is approximately  $10^{-13}$  mho/m. This implies that it would be necessary to maintain a resistance of  $10^{15} \Omega$  between the probes in order to measure the potential difference to a 1% accuracy. For many systems, this is a prohibitively large value. Also, because of capacitance associated with the system, the R.C. time constant tends to be large, and it is difficult to leak excess charge off the probes. Finally, because charge tends to

accumulate on the large, immobile hydrometers, the conductivity inside thunderstorms is at least an order of magnitude ( $< 10^{14}$  mho/m) smaller than the clear air conductivity.

Because of the problems associated with potential probes, we decided to develop an A.C. coupled device. With our instrument, we indirectly determine the electric field by measuring the induced charge flow between symmetric conductors as these conductors change their orientation with respect to the external electric field. While this approach removes the impedance and time constant problems inherent with the D.C. probe, it adds several new constraints. These constraints will be discussed in a later section.

### 3.2 Physical Description

The Balloon Electric Field Sensor (BEFS) consists of a super-pressure spherical balloon, with a conductive metal coating on the outer surface, and the associated electronics package which is mounted inside the balloon. The metallized surface of the balloon is divided into four conducting regions that are electrically isolated from one another on the balloon surface (see Figure 1). Two of these lunular regions are symmetric about the vertical spin axis. The other two are symmetric about the horizontal axis.

These conducting quadrants serve as the sensing elements of the instrument. When the balloon is exposed to an electric field, charge is induced on these conducting surfaces. As the balloon changes its orientation with respect to this field, the induced surface charge is

redistributed. A resulting induction current is measured as it flows through the wires connecting each symmetric lunal pair with electrometer circuits. Since the orientation of the balloon can be determined from on-board sensors, this induction current can be used to calculate the external vector electric field.

Again referring to Figure 1, notice that spin paddles are mounted, one on each side, near the intersections of the quadrant separators. Their position, together with the location of the electronics package, determines the spin axis. Spin is caused by the torque imparted on the spin paddles as the balloon rises. While the rotational period of the balloon depends on the rate of rise, it is on the order of ten seconds.

The quadrant separators shown in Figure 1 serve both to maintain the electrical isolation of the individual quadrants and to reduce rain shorting between quadrants.

A total of four relief valves are mounted on the balloon. Since the balloon is super-pressurized on the ground, the relief valves are necessary in order to allow for sufficient out-gassing during flight. The valves are set to maintain a positive pressure differential of 40 millibars inside the balloon.

In the present design the balloon is ten feet in diameter, displaces 524 cubic feet, and, consequently, can lift a five pound payload to 32,000 feet (9.75 km).

### 3.3 Theory of Operation

As stated previously, the conducting lunes serve as the electric field sensing elements for the instrument. The balloon appears as a conducting sphere to a uniform electric field. This electrostatic problem has been treated in numerous texts (e.g., Stratton, 1941). One solution is worked out in Appendix A.1. This solution shows that the induced surface charge density on the sphere is given by

$$\sigma = 3\epsilon_0 E_0 \cos\theta \quad 3.3.1$$

where  $\sigma$  = surface charge density

$\epsilon_0$  = permittivity of free space ( $8.85 \times 10^{-12}$  f/m)

$\theta$  = angle between the ambient field and a point on the surface of the sphere.

If the electric field vector  $E_0$  is perpendicular to the normal at the center of a conducting lune, then integrating over that lunar surface yields a total induced surface charge of (see Appendix A.2)

$$Q = 3\sqrt{2}/2 \pi\epsilon_0 r^2 E_0 \quad 3.3.2$$

where  $r$  = radius of balloon.

Now, if the center of this particular quadrant is rotated to an arbitrary angle  $\theta$  with respect to the field vector, then the induced surface charge on that quadrant becomes (see Appendix A.3)

$$Q(\theta) = 3\sqrt{2}/2 \pi\epsilon_0 r^2 E_0 \cos\theta \quad 3.3.3$$

Obviously, when the orientation of each quadrant of the balloon changes with respect to  $E_0$ , the magnitude of the induced charge on that quadrant must change. That is, for any  $\frac{\partial \theta}{\partial t}$  there will result a  $\frac{dQ}{dt} = I$ . This induced current is measured as it flows between symmetric quadrant pairs. Once  $\theta(t)$  is determined,  $E_0$  can be calculated.

Referring to Figure 2, we may redefine the direction cosine angle  $\theta$ , which is the angle between  $E$  and the center of the upper lune, in terms of two angles,  $\alpha$  and  $\beta$ . Beta is the angle cosine between the lunar intersection along the positive X-axis and  $E$ . Alpha is the angle produced when  $\beta$  is projected onto the Y-Z plane. The equation then becomes

$$Q_A = C'E_0 \cos\alpha \sin\beta$$

where

$$C' = 3\sqrt{2}/2 \pi \epsilon_0 r^2$$

$$\cos\theta = \cos\alpha \sin\beta \quad 3.3.4$$

Equation 4 represents the total charge induced on the upper lune (Quadrant A in Figure 1). It follows that the induced charge on the other three lunes in terms of  $\alpha$  and  $\beta$  is

$$Q_B = -C'E_0 \cos\alpha \sin\beta$$

$$Q_C = -C'E_0 \sin\alpha \sin\beta$$

$$Q_D = C'E_0 \sin\alpha \sin\beta$$

Differentiating equation 3.3.4 with respect to time yields

$$\frac{dQ_A}{dt} = C' [E \cos\alpha \sin\beta + E_0 (\cos\alpha \cos\beta \dot{\beta} - \sin\alpha \sin\beta \dot{\alpha})] \quad 3.3.5$$

Similarly, the rate of change of individual charge on the other three lunes is given by

$$I_B = -C' \left[ \frac{\partial E'}{\partial t} \cos \alpha \sin \beta + E(\cos \alpha \cos \beta \dot{\beta} - \sin \alpha \sin \beta \dot{\alpha}) \right]$$

$$I_C = -C' \left[ \frac{\partial E'}{\partial t} \sin \alpha \sin \beta + E(\sin \alpha \cos \beta \dot{\beta} + \cos \alpha \sin \beta \dot{\alpha}) \right]$$

$$I_D = C' \left[ \frac{\partial E'}{\partial t} \sin \alpha \sin \beta + E(\sin \alpha \cos \beta \dot{\beta} + \cos \alpha \sin \beta \dot{\alpha}) \right]$$

The upper and lower lunes are connected together through an RC network, as shown in Schematic I of Appendix B. The resistor portion of this network converts the current flowing between the upper and lower lunes into a voltage which is then amplified by an on-board electrometer. It must be noted that currents of opposite signs are flowing in opposite directions through each set of lunes. Hence, the total current flow through the vertical and horizontal resistors is

$$I_V = I_A - I_B = G[\dot{E} \cos \alpha \sin \beta + E(\cos \alpha \cos \beta \dot{\beta} - \sin \alpha \sin \beta \dot{\alpha})] \quad 3.3.6$$

$$I_H = I_C - I_D = G[\dot{E} \sin \alpha \sin \beta + E(\sin \alpha \cos \beta \dot{\beta} + \cos \alpha \sin \beta \dot{\alpha})] \quad 3.3.7$$

where  $I_V$  = total current flow between the vertical pair of lunes,

$I_H$  = total current flow between the horizontal pair of lunes,

$$G = 3\sqrt{2}/2 \pi \epsilon_0 r^2 = 2.74 \times 10^{-10} \text{ farad-meters}$$

(a constant of the system).

The measured voltage drop across each resistor set corresponds to

$$V_{VI} = R_V G [E(\cos \alpha \cos \beta \dot{\beta} - \sin \alpha \sin \beta \dot{\alpha}) + \dot{E} \cos \alpha \sin \beta] \quad 3.3.8$$

$$V_{HI} = R_H G [E(\sin \alpha \cos \beta \dot{\beta} + \cos \alpha \sin \beta \dot{\alpha}) + \dot{E} \sin \alpha \sin \beta]$$

### 3.4 Modes of Operation

It is obvious that we will measure induced charge flow between quadrants whenever  $\alpha$ ,  $\beta$ , or  $E$  change. These parameters will change during a flight for a variety of reasons.

In the fair weather case, since  $E$  changes with altitude, the simple fact that the balloon rises will cause an induced charge to flow. In the thunderstorm, changes in  $E$  due to lightning discharge and charge regeneration will drive currents between quadrants. Whenever the magnitude of  $E$  changes, we measure this charge independent of the relative motion of the balloon.

Induced current flow caused by the angular motion of the balloon can be divided into three different frequency ranges. These various types of motion can be used as separate measurement modes in order to calculate  $\dot{E}$ . The principal modes for the vertical lures are as follows:

$$1) I_V \propto \frac{dE}{dt} = \frac{\partial E}{\partial Z} \frac{\partial Z}{\partial t} = v_z \frac{\partial E}{\partial Z}$$

The induced current is produced by the balloon rising through a gradient electric field. The resulting current appears mainly as a D.C. component of the output.

- 2) Precessional motion - caused by the weight distribution, torque points, and self induced motion of the balloon. This motion tends to have a period on the order of a few seconds and produces an A.C. signal of the same period.

- 3) Forced motion - possibly caused by eddies and turbulence in the wind. This motion is similar to the precessional motion, but it is of lower amplitude and higher frequency. There is a possibility that the voltage output attributed to this motion was actually caused by intermittent contact between the balloon surface and the connection wires. This possibility is explored in Chapter Four.

The modes for the horizontal lunes are:

- 1) Rotational motion - produced by the rising motion of the balloon; has a period on the order of ten seconds.
- 2) Precessional motion - same as for the vertical lunes.
- 3) Forced motion - same as for the vertical lunes.

Any current flow between quadrants that is not produced by the motion of the balloon is caused by an external source. There do exist a number of external sources of current that could possibly cause inaccurate determination of the electric field. These external currents will be discussed in a later section.

### 3.5 Electronics Package

This section contains only a brief description of the BEFS electronics package. A detailed description is available in Appendix B. Figure 3 is a block diagram of the electronics system. The induced current flows through an R.C. network as it passes between quadrant pairs. The R.C. network converts the signal to the voltage mode and acts as a

low pass filter. Both electric field signals are then amplified, compressed in order to increase dynamic range, and sampled every two milliseconds by a 16 channel analog multiplexer. At the same time auxiliary data channels from a pressure sensor, magnetometers, and thermistors are fed to the multiplexer, and each are sampled every eight milliseconds. From the multiplexer, the data is fed through a sample/hold amplifier to a twelve bit analog-to-digital converter. The digitized data then frequency modulates a 1,680 MHz. transmitter, and drives a surface mounted, cavity backed, spiral antenna.

The magnetometers are used for the determination of the balloon orientation. The pressure gauge measures the atmospheric pressure inside the thunderstorm or, if radar tracking fails, serves as an altitude indicator. The external thermometer measures the temperature profile of the thunderstorm, while the internal thermometer supplies housekeeping information. Because of its metallic coating, the balloon is easily tracked by radar except in the most intense rain regions. The 1,680 MHz. transmitter also allows tracking by a standard meteorological rawinsonde receiver. With these auxiliary sensors, not only can the BEFS experiment measure the vector electric field within a thunderstorm, but it can also supply information on the storm's temperature, pressure, and wind structure.

In its present configuration, the field meter is capable of resolving one part in  $2 \times 10^4$ . This 86db dynamic range is ultimately determined by the 12-bit A/D converter and the compressor amplifier. Unfortunately, the total dynamic range of the sensor with respect to electric field measurements may be significantly less than 86db

depending upon the frequency response of the front-end amplifier. Figure 8 shows the frequency response curves of the two amplifier designs.

The output of the voltage amplifier is a function of the current flowing between lunes which, in turn, is a function of the rate of change of the balloon orientation. As described in section 3.4, the frequency at which the balloon changes orientation varies over a wide range (approximately thirty). The frequency dependence of the voltage amp effectively reduces the system's dynamic range to 56db.

As long as the frequency of change in balloon orientation is between 0.05 hz. and 200 hz., the output from the charge amp is essentially frequency independent. Hence, with this amplifier, the total system dynamic range is 86db. The relative merits of these amplifiers is discussed in more detail in a later chapter.

### 3.6 Design Advantages

Several of the BEFS design innovations help to reduce the problems encountered with earlier experiments as described in Chapter 2. A primary benefit of the BEFS design results from its spherical geometry. Because the BEFS field enhancement factor can be calculated directly from theory, no laboratory calibration is necessary. The elaborate, difficult, and error prone calibrations that are necessary with aircraft experiments are thus avoided.

As discussed in Chapter 2, whenever an elongated or pointed conductor is placed in an intense electric field, the probability for

corona discharge is strongly enhanced. Any corona discharge severely distorts the ambient electric field and makes accurate measurements impossible. The spherical shape of the BEFS instrument minimizes this problem, since a sphere produces the smallest possible enhancement factor (equal to 3) in an electric field. The BEFS was designed to have no conductors protruding more than a quarter inch from its spherical surface.

With many balloon borne experiments, static charge build-up on the surface of the balloon distorts the ambient electric field and makes measurements of the vertical profile impossible. When static charge builds up on the surface of the BEFS, it becomes evenly distributed because of the conducting surface; consequently, this excess charge is not redistributed by the balloon motion. For this reason, field measurements using either the precessional or spin modes are not affected by static charge build-up and full vertical profiles can be measured. The metallized surface reduces system weight in that it requires no external electrodes; it also acts as an electric shield protecting the internal electronics from the noise spikes of lightning discharges.

### 3.7 Design Limitations

Every design has its disadvantages. An unfortunate design deficiency of the BEFS is the slow balloon spin rate. One cannot uniquely solve for either the magnitude or direction of  $\vec{E}$  from the precessional or forced modes alone. This is a consequence of the fact that the sensors respond to the full vector field in these modes, yet orientation is known only with respect to vertical. Hence we initially have three

unknowns,  $E$ ,  $\alpha$ , and  $\beta$ ; and only two knowns,  $V_V$  and  $V_H$ . This impasse is removed by the spin mode of the sensor. In the spin mode, only the horizontal components of  $E$  are measured; the vertical component is not sensed. Once  $E_H$  is determined, the precessional and forced modes supply sufficient data to determine  $E$ .

The balloon spins with a period on the order of ten seconds. If the direction of  $E_H$  changes with periods of less than ten seconds, information is lost. (Changes in magnitude are sensed directly at very high speed.) Measurements made by Winn and Byerly (1975) of horizontal field changes due to lightning inside thunderclouds, indicate that changes in the direction of  $E_H$  were generally on the order of tens of degrees or less. The recovery time from these field changes was generally on the order of a minute or more, thus, the BEFS time resolution should be adequate for determining the full features of the typical field change.

### 3.8 External Error Sources

There exist a number of influences which the balloon may encounter during its flight that might result in errors in the electric field measurements. One possible error source is a reduced output voltage due to rain decreasing the resistance between quadrants.

While rising through a thundercloud, the balloon surfaces will become wet. This water could flow across the inflated quadrant separators and reduce the separation resistance. If we assume, once the steady state situation is reached, that the volume of water residing on

the upper lunal surface is equal to that amount of water that is displaced by one quarter of the balloon's volume, then we may calculate the surface thickness of this water. The volume of the displaced water is equal to the surface area of the upper lune times the thickness of the water on the lune. That is, assuming an isotropic drop distribution;

$$\begin{aligned} V_{\text{water}} &= A_{\text{lune}} \times T \\ &= N \times V_D \end{aligned}$$

where  $N$  = number of displaced drops,

$$V_D = \text{mean drop volume} = \frac{4}{3} \pi r^3.$$

$$\text{But, } N = n_D V_Q = \frac{R}{V_D v} V_Q$$

where  $n_D$  = number density of drops,

$$V_Q = \text{quadrant volume} = \frac{\pi}{3} r^3 \text{ lune.}$$

$R$  = rainfall rate,

$v$  = drop fall velocity.

Therefore

$$T = \frac{N V_D}{A_L} = \frac{R(V_Q)}{v(A_L)} = \frac{R}{v} \left( \frac{r}{3} \right).$$

The total rain water resistance between quadrants can be approximated by integrating the rain water resistivity over one complete quadrant separator. Thus,

$$R = \rho' \frac{s}{S}$$

where  $R$  = total rain water resistance

$\rho'$  = circumference of rain separators

$s$  = circumference of rain separators

S = surface area of quadrant separators

= T × length of quadrant separators.

$$\text{Thus } R = \rho' \frac{\pi d}{T(2\pi r)} = \rho' \frac{d}{(R/V \cdot r/3)(2r)}$$

$$R = \frac{\rho' V}{R} \left( \frac{3}{2} \frac{d}{r^2} \right).$$

Typically, in a heavy rainfall,

$$v = 5 \text{ m/sec}$$

$$R = 1.5 \text{ cm/hr} = 4 \times 10^{-6} \text{ m/sec}.$$

Rain water resistivity is typically

$$200 - 300 \Omega\text{-m}.$$

The balloon radius is five feet (60 inches); the separator diameter is one inch. Therefore:

$$R = \frac{(300 \Omega\text{-m}) \times 5 \text{ m/sec}}{(4 \times 10^{-6} \text{ m/sec})} \times \frac{3 \times 1 \text{ in}}{2 \times (60 \text{ in})^2} \times 39.37 \text{ in/m}$$

$$\approx 6 \times 10^6 \Omega.$$

Since the resistance between quadrant pairs is  $10^5 \Omega$ , the error due to water, even during very heavy rains, should amount to only a few percent.

The rising motion of the balloon through a region of net space charge would cause a D.C. "contact current" to flow between the upper and lower lunes. This current would appear similar to the induction current produced by the balloon's rising through a gradient  $E$  field. There is very little information available on the space charge concentrations and

distributions inside thunderclouds. It seems likely that most thunderstorm charge resides on small (10 $\mu$ ) droplets, rather than the large rain drops. If we assume that the average charge on each droplet is  $3 \times 10^{-17}$  coul. (Takahashi, 1973), and that the droplet concentration is  $10^9/\text{m}^3$ , then the maximum possible net space charge is  $3 \times 10^{-9}$  coul/m $^3$ . Typically one would expect the net space charge to be at least an order of magnitude less than this, or approximately  $10^{-10}$  coul/m $^3$ .

As the balloon rises through the net space charge, a contact current flows between the vertical quadrants. The current is equal to the net space charge times the rise velocity times the quadrant vertical cross-section. Or,

$$\begin{aligned} I_c &= \rho v A \leq (3 \times 10^{-9} \text{C/m}^3)(5 \text{ m/s})(5 \text{ m}^2) \\ &\leq 7.5 \times 10^{-8} \text{ amps; or, more likely,} \\ I_c &\sim 2 \times 10^{-9} \text{ amps.} \end{aligned}$$

Vertical electric field measurements by Latham and Stow (1969) indicate that electric field gradients of 20 v/m $^2$  are not uncommon. Obviously much larger and much smaller fields will be encountered, but 20 v/m $^2$  may be a reasonable value for the electrically active regions of thunderclouds. If the BEFS is rising at 5 m/sec through a 20 v/m $^2$  vertical gradient, the induction current output from the vertical sensor is

$$\begin{aligned} I_I &= Gv \frac{\partial E}{\partial t} \\ &= 2.74 \times 10^{-8} \text{ amps.} \end{aligned}$$

Thus the two currents differ by an order of magnitude. In fact, the ratio

of gradient current to contact current is given by

$$I_i / I_C = \frac{3\pi\epsilon_0 \sqrt{2}/2 r^2 v \partial E_r / \partial z}{\sqrt{2}/2 \pi r^2 v \rho}$$

$$= \frac{3\epsilon_0 \partial E_r / \partial z}{\rho} \approx 10.$$

Fortunately, even though these currents are of similar amplitudes, the precessional and forced measurement modes will provide accurate electric field data. The motion of the balloon modulates the electric field measurement but has little effect on the contact current. In fact, by determining  $\vec{E}$  from the balloon motion, one could calculate  $\partial E_r / \partial z$  and deduce the net space charge around the balloon.

True conduction (current caused by ions) also presents a potential error source. The conduction current density is given by

$$\vec{J} = \lambda \vec{E}$$

where  $\lambda$  = conductivity of the air.

Thus the total conduction current flow through the vertical lunes is given by

$$I_{CV} = 3\pi \sqrt{2}/2 r^2 \lambda E \cos\theta$$

where  $\lambda$  = angle between center of upper lune and  $\vec{E}$ .

Similarly, the conduction current flow through the horizontal lunes is

$$I_{CH} = 3\pi \sqrt{2}/2 r^2 \lambda E \sin\theta .$$

Recall that the induced current flow through the vertical and horizontal lunes is given by

$$I_{IV} = 3\pi^{1/2} \epsilon_0 r^2 E \sin\theta \dot{\theta}$$

$$I_{IH} = 3\pi^{1/2} \epsilon_0 r^2 E \cos\theta \dot{\theta}$$

Taking ratios of conduction currents to induction currents such that the angle dependence drops out, leaves us with

$$\begin{aligned} \frac{I_{CV}}{I_{IH}} &= \frac{\lambda}{2\epsilon_0} \frac{1}{\dot{\theta}}, & \frac{I_{CH}}{I_{IV}} &= -\frac{\lambda}{2\epsilon_0} T \\ & & &= \frac{\lambda}{2\epsilon_0} T \end{aligned}$$

where  $T$  = period of a particular balloon motion.

For precessional motion,  $T$  is typically three seconds. In the clear air conductivity is

$$\begin{aligned} \text{at sea level} &= 10^{-13} / \Omega\text{-m} \\ 5 \text{ km.} &= 6 \times 10^{-13} / \Omega\text{-m} \\ 15 \text{ km.} &= 10^{-12} / \Omega\text{-m} . \end{aligned}$$

$$\begin{aligned} \text{Then, } \frac{(I_C)}{(I_I)}_{z=0} &\approx 10^{-2} \\ \frac{(I_C)}{(I_I)}_{z=0} &\approx 6 \times 10^{-2} \\ \frac{(I_C)}{(I_I)}_{z=15} &\approx 10^{-1} . \end{aligned}$$

Since the conductivity in a thunderstorm is reduced by at least a factor of ten (Rusk and Moore, 1974), these errors would be reduced by the same factor.

## CHAPTER IV

### Test Flight

#### 4.1 Initial Flight

We originally planned for BEFS to enter a thunderstorm on her virgin flight. The Federal Aviation Agency promptly squashed these plans, even though BEFS was designed to comply with FAA Regulation 101.1(4). The agency used its "Hazardous Operation" catch-all, claiming that, while inside a thunderstorm, the BEFS would be hazardous to aircraft. After months of negotiation, the FAA finally allowed a fair weather flight. We still have not been able to make a thunderstorm flight.

The BEFS was launched at 16:29 CDT on 17 May 1974, from the NCAR Balloon Facility near Palestine, Texas (see Figure 4). At the time of launch, there were scattered cumulus clouds in the vicinity of Palestine, but radar indicated no thunderstorm activity in the area. The balloon reached a maximum altitude of 8.3 km. approximately forty minutes after launch. The total flight duration was 1 hour and 35 minutes. Figure 35 shows the altitude, pressure, and temperature profiles during the flight. The low maximum altitude resulted from the weight imposed by the positive recovery system and from the fact that a certain amount of air was introduced into the balloon prior to launch. The positive recovery system was a result of FAA requirements.

This first flight was primarily intended to be a design test. Naturally we also wished to measure the fair weather electric field as a function of height. The primary goal was fully realized: a number of design problems were uncovered. However, because of these design problems, the secondary goal was not completely achieved.

#### 4.2 Problem Areas

Results from this first flight disclosed four areas requiring modification before a second launch is attempted. Proposed solutions to these problems will be detailed in Chapter 5. Each of these problems will be discussed here.

It is evident from Figure 5 that the external thermistor gave false measurements during the high altitude/cold temperature portions of the flight. The minimum temperature ( $-2^{\circ}\text{C}$ ) indicated by the thermistor corresponds closely with the point of maximum power dissipation by the thermistor and the point where the balloon ascent rate slowed.

Power dissipated in the thermistor causes self-heating and tends to make the thermistor read high. Since the thermistor is mounted at the bottom of the balloon, it receives very poor air circulation when the balloon is stationary or rising slowly. The combination of poor air circulation and heating of surrounding air by the thermistor probably accounts for the inaccurate measurements.

During the flight, the on-board digital clock tended to drift in frequency as a function of temperature. The NCAR decommutator had a very narrow frequency tolerance. The consequence of these factors was a

number of synchronization losses during the flight. In the future, we will use a quartz controlled clock and our own decommutator.

The most serious problem encountered during the flight involved the orientation detectors. The individual magnetometers were not sensitive enough to measure the small rapid changes that caused large dominant outputs from the electric field sensors. At the same time, the orientation system, as a whole, could not give unique solutions of the balloon orientation. Because of these problems, we cannot uniquely determine  $\alpha$ ,  $\beta$ ,  $\dot{\alpha}$ , or  $\dot{\beta}$ ; consequently, we cannot directly solve for  $E$ . The following section discusses this problem in more detail.

In addition to the above mentioned problems, the balloon itself may have contributed to errors encountered during the initial flight. Because of excess handling, the balloon developed many minute cracks in its conductive coating. These cracks effectively electrically isolated certain surface areas from each other. Conductive paint was used to reduce this isolation; however, this operation was only partially effective. If any isolated area developed during the flight, the electrical response of the BEFS would have been altered.

Prior to launching the balloon, we checked the connections between each conducting lute and its lead wire. The connections were good only when the BEFS was rigidly inflated; this was considered acceptable at the time. Later investigations indicated that the conducting epoxy, which was used to electrically connect the leads to the surfaces, tended to crack with age. It is possible that a number of the connections to the balloon surface were intermittent and, consequently, introduced noise spikes into the system. Such noise spikes might explain the great

dispersion in the calculated electric field values.

The orientation system and the electrometer response will be modified for the next flight. Surface conductivity will be insured prior to the next flight.

### 4.3 Data Analysis

The forced motion measurement mode (see Chapter 3.4) totally dominated the electric field detector outputs. All other modes were buried in this high frequency "noise." The balloon motions that generated these outputs were of high frequencies, but of low amplitudes. In fact, the balloon forced mode angular changes were so small that they often were less than the change necessary to produce a change in the least significant bit on the output of one of the magnetometers. Because of this and the lack of exact orientation information, data reduction has been difficult. Three approaches have been attempted.

#### 4.3.1 Low-Pass Filter

The first approach was to run the data through a digital low-pass filter. It was hoped that, by low-pass filtering the data, the contributions from the forced mode could be removed. In order to effectively remove the effects of the forced mode motion, it would be necessary to reduce the high frequency cut-off to below one Hertz. Unfortunately, since the BEFS was designed to provide good time resolution on lightning events, the sampling rate was once every two milliseconds on both the horizontal and vertical detectors. A 256 point low-pass filter would be required to accurately remove all frequencies above 1 Hz. from data

sampled at this rate. Such a filter is prohibitively long. Instead, a 64 point finite impulse response filter was generated from a program written by Jim McClennan of Rice University.

In order to save computer time, fixed point values of the filter elements were combed through the BEFS data in such a manner that every eighth data point was retained. A total of three passes were made through the data. The data was renormalized after each pass. Unfortunately due to the use of fixed point notation, by the third pass so much significance was lost from the data that quantitative analysis was impossible. Furthermore, time shifts became so large that correlation between the electric and magnetic field data was difficult. For these reasons attempts to analyze the low frequency portion of the data via low-pass filtering were temporarily abandoned. At a later time, we plan to convert to floating point notation and, with a faster computer, try the filter technique again.

#### 4.3.2 Differentiating the Orientation Data

In the next analysis procedure, a series of assumptions were made in an attempt to remove the angular dependence from the electric field data. Referring to Figure 2, the three components of the electric field with respect to the balloon are

$$\begin{aligned} E_x &= E_0 \cos\beta \\ E_y &= E_0 \sin\alpha \sin\beta \\ E_z &= E_0 \cos\alpha \sin\beta \end{aligned} \tag{4.3.1}$$

The electric field component along the x-axis does not induce any net charge on any of the lunes (symmetry).

If we integrate over each lunar pair, we find as before,

$$\begin{aligned} Q_y \equiv Q_H &= G' E_0 \sin\alpha \sin\beta, \\ Q_z \equiv Q_V &= G' E_0 \cos\alpha \sin\beta. \end{aligned} \quad 4.3.2$$

Differentiating these equations (for constant E) gives

$$\begin{aligned} V_V &= I_V R = R \dot{Q}_V = G E_0 (\cos\alpha \cos\beta \dot{\beta} - \sin\alpha \sin\beta \dot{\alpha}), \\ V_H &= I_H R = R \dot{Q}_H = G E_0 (\sin\alpha \cos\beta \dot{\beta} + \cos\alpha \sin\beta \dot{\alpha}). \end{aligned} \quad 4.3.3$$

Taking the sum of the squares yields

$$V_V^2 + V_H^2 = G^2 E_0^2 (\cos^2\beta \dot{\beta}^2 + \sin^2\beta \dot{\alpha}^2). \quad 4.3.4$$

If we now assume that the fair weather electric field is vertical and that, on the average, the balloon orientation is close to the vertical, then to a first approximation  $\beta \approx 90^\circ$  and

$$V_V^2 + V_H^2 = G^2 E_0^2 \dot{\alpha}^2. \quad 4.3.5$$

If we set up exactly the same coordinate system with respect to the earth's magnetic field, then

$$\begin{aligned} B_x &= B_0 \cos\beta_B, \\ B_y &= B_0 \sin\alpha_B \sin\beta_B, \\ B_z &= B_0 \cos\alpha_B \sin\beta_B. \end{aligned} \quad 4.3.6$$

Taking the derivatives with respect to time,

$$\begin{aligned}
 \dot{B}_x &= -B_0 \sin\beta_B \dot{\beta}_B \\
 \dot{B}_y &= B_0 (\cos\beta_B \sin\alpha_B \dot{\beta}_B + \cos\alpha_B \sin\beta_B \dot{\alpha}_B) \\
 \dot{B}_z &= B_0 (\cos\alpha_B \cos\beta_B \dot{\beta}_B - \sin\alpha_B \sin\beta_B \dot{\alpha}_B)
 \end{aligned}
 \tag{4.3.7}$$

If we take the sum of the squares of the y and z components, we get

$$\dot{B}_y^2 + \dot{B}_z^2 = B_0^2 (\cos^2\beta_B \dot{\beta}_B^2 + \sin^2\beta_B \dot{\alpha}_B^2),
 \tag{4.3.8}$$

Further, if we make our measurement when

$$\dot{B}_x = B_0 \cos\beta_B = 0$$

then the equation becomes

$$\dot{B}_y^2 + \dot{B}_z^2 = \dot{B}_0^2 \dot{\alpha}_B^2 \quad (\beta_B \approx 90^\circ)
 \tag{4.3.9}$$

Both  $\dot{\alpha}$  and  $\dot{\alpha}_B$  are the angular velocity components of the balloon about its x-axis and are thus approximately equal. Hence,

$$\frac{V_V^2 + V_H^2}{G^2 E_0^2} \approx \frac{B_y^2 + B_z^2}{B_0^2}
 \tag{4.3.10}$$

or

$$E_0 \approx B_0/G \sqrt{\frac{V_V^2 + V_H^2}{B_y^2 + B_z^2}}.
 \tag{4.3.11}$$

We used this approximation to make calculations of the electric field magnitudes every four to five seconds during the rising portion of the flight. On the average the results seem reasonable, but the dispersion is very large.

There are two primary factors that contribute to the large errors. The largest errors result when  $\dot{\alpha}$  becomes very small, and, consequently,  $E_0$  in Eq. 4.3.11 becomes very large. This happens because the approximation that lead to Eq. 4.3.5 breaks down for small  $\dot{\alpha}$ . Since  $\beta = \pi/2 + \Delta\beta$ , where  $\Delta\beta$  although small is generally not zero, Eq. 4.3.4 may be rewritten

$$V_V^2 + V_H^2 = G^2 E_0^2 [\sin^2(\Delta\beta) \dot{\beta}^2 + \cos^2(\Delta\beta) \dot{\alpha}^2] \quad 4.3.12$$

This immediately implies that our approximation fails when

$$\cos(\Delta\beta) \dot{\alpha} \gg \sin(\Delta\beta) \dot{\beta}$$

Unfortunately we cannot uniquely determine either  $\Delta\beta$  or  $\dot{\beta}$ . To the first order,  $\dot{\beta}$  is the balloon angular velocity about its y-axis. We can get an approximate value for  $\dot{\beta}$  by calculating  $\alpha_B$  from  $\tan(\alpha_B) = B_y/B_z$ , and by assuming that  $\dot{\beta}_B$  is the projection of  $\dot{\beta}$  onto its rotational plane. That is, the x-axis magnetometer is sensitive, in the B field coordinate system, to only a portion of the rotation about the y-axis, or

$$\dot{\beta}_B \sim \cos\alpha \dot{\beta} \quad 4.3.13$$

There is no way to estimate  $\Delta\beta$ . All we can do is assume that, since motion about either the x or y axis is equally probable,

$\overline{(\Delta\beta)_x} = \overline{(\Delta\beta)_y}$ . The magnetic dip angle near Houston is  $30.7^\circ$ ; therefore,

$$|(\Delta\beta)_y| \approx |\alpha_B - 30.7^\circ| = |\tan^{-1}(B_y/B_z) - 30.7^\circ|$$

Thus, we assume that

$$|\Delta B_x| = |\tan^{-1}(B_y/B_z) - 30.7^\circ|$$

Plugging these values back into Eq. 4.3.12, we get

$$\begin{aligned} V_V^2 + V_H^2 &\approx G^2 E_0^2 \left\{ \left[ \tan^{-1}(B_y/B_z) - 30.7^\circ \right]^2 \frac{B_x^2}{\cos^2(\tan^{-1} B_y/B_z)} \right. \\ &\quad \left. + \left[ 1 - (\tan^{-1}(B_y/B_z) - 30.7^\circ)^2 \right] \left[ \dot{B}_y^2 + \dot{B}_z^2 \right] \right\} \\ &\approx \frac{G^2 E_0^2}{B_0^2} \left\{ (B_y/B_z - 0.5358)^2 (\frac{1}{3} \dot{B}_x^2) + \dot{B}_y^2 + \dot{B}_z^2 \right\} \end{aligned}$$

or

$$E_0 = \frac{B_0}{G} \sqrt{\frac{V_V^2 + V_H^2}{\frac{1}{3} (B_y/B_z - 0.5358)^2 \dot{B}_x^2 + \dot{B}_y^2 + \dot{B}_z^2}}$$

4.3.14

We calculated a number of  $E_0$  values using Equation 4.3.14. The results were better than those calculated using Equation 4.3.11, but were still highly dispersive. This is not surprising since  $\beta$  is poorly known. It might be possible to get a better handle on  $\beta$  by inserting values of  $E_0$ , calculated from Equation 4.3.14, into Equation 4.3.12 and solving for  $\beta$ . By iterating in this manner, accurate values for both  $\beta$  and  $E_0$  might be obtained. This procedure has not been tried.

Another factor contributing to the large dispersion encountered with this model is the inaccuracies in the determination of  $\dot{B}_x$ ,  $\dot{B}_y$  and  $\dot{B}_z$ . As mentioned previously, the forced mode seemed to cause most of

the electrometer output voltage. In this mode the balloon suffered rapid but small angular changes. These changes tended to be smaller than would be necessary for a change of one bit on the digitized magnetometer outputs. Because these changes were at the limit of the magnetometers to sense them, differentiation of the magnetometer data tended to be noisy. Inaccurate values of  $\dot{B}_x$ ,  $\dot{B}_y$ , and  $\dot{B}_z$  caused inaccurate determinations of  $E$ .

As alluded to earlier, there also exists the possibility that the large dispersion in calculated field values was a consequence of poor surface conductivity and/or intermittent contacts between the surfaces and the electrometer leads. Obviously, any voltage outputs that were not caused by changes in balloon orientation would yield totally unreasonable field values.

Figure 6 shows a number of electric field values calculated from the data using Equation 4.3.14. Because of the high dispersion and lack of confidence in these results, only two selected periods during the flight were analyzed. Further analysis was not considered expedient.

The dashed line in Figure 6 was plotted using an empirical equation originally expressed by Gish (1944).

#### 4.3.3. Integrating the Electric Field Data

By numerically integrating the voltage output of the electric field sensors over definite time intervals, the forced motion angular velocity dependence can be reduced. Then Equation 4.3.8 becomes

$$V_V \Big|_{t_1}^{t_2} = R G E_0 \left[ \int_{t_1}^{t_2} \left( \cos \alpha \cos \beta \frac{\partial \beta}{\partial t} dt - \sin \alpha \sin \beta \frac{\partial \alpha}{\partial t} dt \right) \right]$$

$$V_{IV} = R G E_0 \left[ \cos \alpha (\sin \beta_2 - \sin \beta_1) + (\cos \alpha_2 - \cos \alpha_1) \sin \beta \right]. \quad 4.3.15$$

Likewise

$$V_{IH} = R G E_0 \left[ \sin \alpha (\sin \beta_2 - \sin \beta_1) + (\sin \alpha_2 - \sin \alpha_1) \sin \beta \right].$$

Let

$$\alpha = \frac{1}{2}(\alpha_1 + \alpha_2)$$

$$\beta = \frac{1}{2}(\beta_1 + \beta_2)$$

$$\Delta \alpha = \frac{1}{2}(\alpha_2 - \alpha_1)$$

$$\Delta \beta = \frac{1}{2}(\beta_2 - \beta_1)$$

where  $\alpha$  and  $\beta$  are defined as points in the integration interval, and  $\Delta \alpha$  and  $\Delta \beta$  are the difference between these angles and angles at the ends of the interval. Inserting these angles into Equation 4.3.15 yields

$$V_{IV} = 2 R G E_0 \left[ \cos \alpha \cos \beta \sin(\Delta \beta) - \sin \alpha \sin \beta \sin(\Delta \alpha) \right]$$

$$V_{IH} = 2 R G E_0 \left[ \sin \alpha \cos \beta \sin(\Delta \beta) + \sin \alpha \sin \beta \sin(\Delta \alpha) \right].$$

Taking the sum of the squares:

$$V_{IV}^2 + V_{IH}^2 = 4 R^2 G^2 E_0^2 \left[ \cos^2 \beta \sin^2(\Delta \beta) + \sin^2 \beta \sin^2(\Delta \alpha) \right]. \quad 4.3.16$$

This equation is very similar to Equation 4.3.4 and, consequently, presents

the same analysis difficulties. The major advantage associated with Equation 4.3.16 is that the integration period may be varied at will. In this way relatively large angle changes can be used. The inaccuracies associated with differentiating the magnetometer data are eliminated. Of course there are errors in determining  $\Delta\alpha$  and  $\Delta\beta$ , but these errors tend to be relatively smaller than the errors due to differentiation.

For  $\Delta\alpha, \Delta\beta$  (small), we may rewrite Equation 4.3.16 as

$$\begin{aligned} V_{IV}^2 + V_{IH}^2 &= 4 R^2 G^2 E_0^2 \left[ \cos^2 \beta (\Delta\beta)^2 + \sin^2 \beta (\Delta\alpha)^2 \right] \\ &= 4 G^2 R^2 E_0^2 \left[ \cos^2 \beta (\beta_2 - \beta_1)^2 + \sin^2 \beta (\alpha_2 - \alpha_1)^2 \right] \end{aligned} \quad 4.3.17$$

recalling that

$$\begin{aligned} B_x &= B_0 \cos \beta_B \\ B_y &= B_0 \sin \beta_B \cos \alpha_B \\ B_z &= B_0 \sin \beta_B \sin \alpha_B . \end{aligned}$$

For points where  $B_x$  is small:

$$V_{IV}^2 + V_{IH}^2 \approx \frac{R^2 G^2 E_0^2}{B_0^2} \left[ B_x^2 (\beta_2 - \beta_1)^2 + (B_y^2 + B_z^2) (\alpha_2 - \alpha_1)^2 \right].$$

We further assume that:

$$\alpha = |\alpha_B - 30.7^\circ|. \quad (30.7 = \text{dip angle at Houston})$$

Then, since  $\tan \alpha_B = B_y / B_z \approx \alpha_B$ , we have

$$(\alpha_2 - \alpha_1)^2 \approx \left( \frac{B_{y_2}}{B_{z_2}} - \frac{B_{y_1}}{B_{z_1}} \right)^2 .$$

When the measurements are taken for only small  $B_x$ , the equation simplifies to

$$V_{IV}^2 + V_{IH}^2 \approx \frac{R^2 G^2 E_0^2}{B_0^2} \left[ (B_y^2 + B_z^2) \left( \frac{B_{y_2}^2}{B_{z_2}^2} - \frac{B_{y_1}^2}{B_{z_1}^2} \right) \right] \quad 4.3.18$$

Because of the comparatively long integration period this approximation tends to be better than the equivalent approximation which led to Equation 4.3.12.

Rearranging terms yields

$$E_0 = \frac{G'}{\left( \frac{B_{y_2}}{B_{z_2}} - \frac{B_{y_1}}{B_{z_1}} \right)} \sqrt{\frac{V_{IH}^2 + V_{IV}^2}{B_y^2 + B_z^2}} \quad 4.3.19$$

or

$$E_0 = \left( \frac{B_{z_1} B_{z_2} G'}{B_{y_2} B_{z_1} - B_{y_1} B_{z_2}} \right) \sqrt{\frac{V_{IH}^2 + V_{IV}^2}{B_y^2 + B_z^2}}$$

A smoothed electric field profile calculated from this technique is shown in Figure 7. Because of unreliability due to the high dispersion of the raw field values, clipping of the data during the early portion of the flight, and loss of sync later in the flight, only a small segment of the flight is presented.

## CHAPTER V

### The Next Flight

This chapter details the changes that are being tested in order to improve the instrument for the next flight. It indicates what we hope to accomplish in the next flight and what should be done in the future.

#### 5.1 Instrument Modifications

A number of modifications are being tested. In order to improve data recoverability, a change in the digital clock and the digital code are being implemented. A new transmitter is being considered.

As long as the external thermometer is mounted at the bottom surface of the balloon, poor air circulation will potentially cause errors in the temperature measurements. Since the system design requires that the temperature sensor remain at its present location, the sensor itself must be modified. Replacement by a thermocouple or RTD would be reasonable, but since the thermistors are already in-house, we will still try to use them. By reducing the current flow through the thermistor, self-heating can be decreased and more accurate measurements might be obtained. Laboratory tests will be run to accurately check the thermistor self-heating effect at low temperature.

The balloon orientation detector must be redesigned. We expect to replace the present tri-axial magnetometer with a system comprised of two pendulum inclinometers and two magnetometers. The inclinometers

mounted at right angles to each other, will measure the inclination of the balloon about the x and y axes. The magnetometers, mounted along the x and y axes, will measure the azimuth of the balloon with respect to north. This system is in the testing stage.

In order to decrease the effect of the forced motion mode, the front end amplifier is being redesigned. In the present design, the amplifier measurement is proportional to the balloon angular velocity (see Figure 8), as well as to the balloon orientation and the changing electric field.

The system has a total dynamic range of  $10^4$ . The range in intensities of the electric fields that we wish to measure is  $10^4$ . Unfortunately, the range in balloon angular velocities that we used in making our measurements is greater than thirty. Obviously, not only is the data analysis made complicated by the dependence on balloon angular velocity, but the system's effective dynamic range is reduced.

By replacing the present current amplifier with a charge amplifier, the output dependence on the balloon angular velocity is removed (see Figure 8). This change to a charge amplifier on the front end should simplify the data analysis and increase the effective dynamic range of the instrument. Furthermore the use of a charge amplifier, because of its high frequency cut-off, should provide improved protection against large electric field changes.

## 5.2 Flight Objectives

The primary objectives of the BEFS were discussed in Chapters I and II. Basically, on the next flight, we wish to measure accurately the vector electric field inside a thunderstorm. Determination of the variation of the vector field as a function of temperature and altitude is a principal goal. Such data would provide a gross picture of the electrical structure in the thunderstorm, aid in the determination of charged regions, and help in the development of an electrified cloud model.

A great deal of additional information should become available from the next flight.

- 1) Radar and GMD tracking of the balloon should provide information on the location of the balloon within the storm, and on the relative winds in the vicinity of the balloon.
- 2) Radar information from high reflection regions of the cloud should provide information on the cloud dynamics. If the BEFS should enter a high reflection region, we would have information on the relative electric fields inside and outside these regions. This information would prove valuable in determining the relative importance of large drops in the charge generation process.
- 3) Electric field and electric field change data will be available for correlation with the BEFS in-situ field measurements. Measurements taken just before and after the BEFS enters the cloud base should provide information on the characteristics of the screening layer and on the difference in conductivity in the clear air and in

the cloud.

4) Comparison of electric field changes measured by BEFS and measured at the ground should provide information on the relative field recovery characteristics. It should also provide information on the net charge in the region that produced the lightning discharge (Winn and Byerly, 1975).

5) It is hoped that we will have available a ground based acoustic array station as described by Few (1975). With such a system, it is possible to reconstruct acoustically the path of the lightning channel within the cloud. If the location of the BEFS is known in relation to the discharge region of the cloud as determined from acoustic reconstruction, and if the vector electric field at the balloon location is accurately measured, then information on the location of the charged region, the magnitude of the charge in this regions, and the dimensions of this region could be deduced.

In summary, if successful, the next BEFS flight should provide a profile of the electric field structure within a thundercloud. It should provide information on the characteristics of the charged regions within the cloud. By correlating these measurements with the dynamic structure of the cloud, we hope to make a definitive contribution toward unravelling the charge generation and separation mechanisms driven within the thundercloud. Naturally the thunderstorm is too complex and devious to reveal herself to a single probe; however, under coordinated attacks from many experiments, she may, blushing, expose her secrets.

## ACKNOWLEDGEMENTS

I am indebted to my advisor, Dr. Arthur Few, for suggesting this project, for valuable discussions and for that occasional push during the data reduction phase. I wish to thank Drs. Anderson and Freeman for taking the time to serve as members of my committee. I am truly grateful to Michael Stewart who, as project engineer, designed and built much of the payload electronics. We went through quite a learning process together.

I am grateful to my parents for stimulating my first interest in science and for revealing the value of education. My beautiful wife Candice has been a constant source of encouragement and help. Her smile brightens the darkest problems.

I thank Anita Poley for typing this manuscript and G.T. Scheldahl, Co. for building the balloons. I appreciate the support and patience demonstrated by Mr. James Hughes and Cmd. William Smith.

This project has been supported by the Atmospheric Program of the Office of Naval Research under Contract Number N00014-75-C-0139 NR211-191. Additional support was received from the National Aeronautics and Space Administration SR & T Grant NGL 44-006-012. Patent number 3,925,726 has been granted on the BEFS design.

## APPENDIX A

### A.1 Conducting Sphere in an Electric Field

Following the procedure outlined in Stratton (1942), consider the situation shown in Figure 9. There is a conducting sphere of radius  $a$ , whose center is located at the origin of the coordinate system. At  $Z = Z_1 > a$  (on the  $Z$ -axis), there is located a point charge  $q$ . Let  $V_0$  be the potential due to the source charge  $q$  and  $V_1$  be the potential due to the charge distribution on the sphere. The resultant potential at any point outside the sphere is  $V = V_0 + V_1$ .

The primary potential at point  $P$  is  $V_0 = q/(4\pi\epsilon_0 r_1)$ . We wish to express this potential in terms of the coordinates of  $P$  with respect to the origin. First it is necessary to express the location  $P$  in terms of the polar coordinates  $r$  and  $\theta$ . Then

$$r_1 = \sqrt{r^2 + Z_1^2 - 2r Z_1 \cos\theta}$$

or

$$\frac{1}{r_1} = \frac{1}{Z_1 \sqrt{1 + (r/Z_1)^2 - 2 r/Z_1 \cos\theta}}$$

If  $|(r/Z_1)^2 - 2r/Z_1 \cos\theta| < 1$ , then we may expand the quantity under the square root by the binomial theorem, such that

$$\frac{1}{r_1} = \frac{1}{Z_1} \left\{ 1 + \frac{1}{2} \left[ \left( \frac{r}{Z_1} \right)^2 - \frac{2r}{Z_1} \cos\theta \right] + \frac{1}{2} \frac{(3/2)}{2!} \left[ \left( \frac{r}{Z_1} \right)^2 - \frac{2r}{Z_1} \cos\theta \right]^2 + \dots \right\}$$

and rearranging

$$\begin{aligned} \frac{1}{r_1} &= \frac{1}{Z_1} \left[ 1 + \frac{r}{Z_1} \cos\theta + \left(\frac{r}{Z_1}\right)^2 \left(\frac{3}{2} \cos\theta - \frac{1}{2}\right) + \dots \right] \\ &= \frac{1}{Z_1} \sum_{n=0}^{\infty} P_n(\cos\theta) \left(\frac{r}{Z_1}\right)^n . \end{aligned}$$

The coefficients of  $r/Z_1$  are the Legendre polynomials

$$P_0(\cos\theta) = 1$$

$$P_1(\cos\theta) = \cos\theta$$

⋮

Therefore, in terms of our coordinate system

$$V = \frac{q}{4\pi\epsilon_0 Z_1} \sum_{n=0}^{\infty} P_n(\cos\theta) \left(r/Z_1\right)^n .$$

We now wish to determine the potential  $V_1$  due to the induced charge on the sphere. Since there is no net charge, we may apply the Laplacian

$$\nabla^2 V_1 = \frac{1}{r^2} \frac{\partial}{\partial r} \left( r^2 \frac{\partial V_1}{\partial r} \right) + \frac{1}{r^2} \frac{1}{\sin\theta} \frac{\partial}{\partial \theta} \left( \sin\theta \frac{\partial V_1}{\partial \theta} \right) + \frac{1}{r^2} \frac{1}{\sin\theta} \frac{\partial^2 V_1}{\partial \phi^2} = 0 .$$

Because we have symmetry about the  $Z$ -axis

$$\frac{\partial V_1}{\partial \phi} = 0 .$$

Therefore

$$\frac{\partial}{\partial r} \left( r^2 \frac{\partial V_1}{\partial r} \right) = - \frac{1}{\sin\theta} \frac{\partial}{\partial \theta} \left( \sin\theta \frac{\partial V_1}{\partial \theta} \right) .$$

Using standard separation of variable techniques, by substituting  $V_1(r, \theta) = R(r) \Theta(\theta)$  and dividing through by  $R(r)\Theta(\theta)$ , we have

$$\frac{1}{R} \frac{d}{dr} \left( r^2 \frac{dR}{dr} \right) + \frac{1}{\Theta \sin \theta} \frac{d}{d\theta} \left( \sin \theta \frac{d\Theta}{d\theta} \right) = 0.$$

Because the variables are separated, we may set each term equal to a constant. Then

$$\frac{d}{dr} \left( r^2 \frac{dR}{dr} \right) - \left[ \ell(\ell+1) \right] R = 0$$

$$\frac{1}{\Theta \sin \theta} \frac{d}{d\theta} \left( \sin \theta \frac{d\Theta}{d\theta} \right) + \ell(\ell+1) \Theta = 0.$$

Substituting  $\cos \theta = X$  into the second equation, and rearranging both gives

$$\frac{d^2 R}{dr^2} + \frac{2}{r} \frac{dR}{dr} - \frac{\ell(\ell+1)}{r^2} R = 0$$

$$(1-X^2) \frac{d^2 \Theta}{dX^2} - 2X \frac{d\Theta}{dX} + \ell(\ell+1) \Theta = 0$$

The first equation is Laplace's equation and has the set of solutions

$$R = \left\{ \begin{array}{l} r^\ell \\ r^{-(\ell+1)} \end{array} \right\}$$

The second equation is the Legendre equation and has the solutions

$$\Theta = \left\{ \begin{array}{l} P_\ell(\cos \theta) \\ Q_\ell(\cos \theta) \end{array} \right\}$$

Now,  $Q_\ell(\cos \theta)$  is a many valued function and may thus be eliminated from the set of solutions. We are thus left with

$$V_1 = \sum_{\ell=0}^{\infty} \left[ a_{\ell} r^{\ell} + \frac{b_{\ell}}{r^{(\ell+1)}} \right] P_{\ell}(\cos\theta)$$

where  $a_{\ell}$ ,  $b_{\ell}$  are arbitrary constants.  $V_1$  must be regular at infinity. This requires that we set  $a_{\ell} = 0$ . The potential of the induced distribution is, therefore, represented by the series

$$V_1 = \sum_{\ell=0}^{\infty} \frac{b_{\ell}}{r^{(\ell+1)}} P_{\ell}(\cos\theta)$$

The resultant potential at any point  $P$  outside the sphere is then

$$\begin{aligned} V = V_0 + V_1 &= \frac{q}{4\pi\epsilon_0 Z_1} \sum_{\ell=0}^{\infty} P_{\ell}(\cos\theta) (r/Z_1)^{\ell} + \sum_{\ell=0}^{\infty} \frac{b_{\ell}}{r^{\ell+1}} P_{\ell}(\cos\theta) \\ &= \sum_{\ell=0}^{\infty} \left[ \frac{q}{4\pi\epsilon_0 Z_1} (r/Z_1)^{\ell} + \frac{b_{\ell}}{r^{(\ell+1)}} \right] P_{\ell}(\cos\theta) \end{aligned}$$

The potential at the surface of the sphere ( $r = a$ ) must be a constant:

$V_S$ . Or,

$$V_S = \sum_{\ell=0}^{\infty} \left[ \frac{q}{4\pi\epsilon_0 Z_1} (a/Z_1)^{\ell} + \frac{b_{\ell}}{a^{(\ell+1)}} \right] P_{\ell}(\cos\theta) = \text{const.}$$

Since, at the surface,  $V_S$  cannot be a function of  $\theta$ , the coefficients of  $P_{\ell}(\cos\theta)$  must vanish for all values of  $\ell$  greater than zero. We are left with

$$V_S(r=a) = \frac{q}{4\pi\epsilon_0 Z_1} (a/Z_1) + \frac{b_0}{a}$$

or

$$b = aV_S - \frac{q}{4\pi\epsilon_0} \frac{a}{Z_1}$$

and

$$b_{\ell} = - \frac{q}{4\pi\epsilon_0} \frac{a^{2\ell+1}}{(Z_1)^{\ell+1}}$$

Hence, at any point at distance  $r$  outside the sphere

$$V = \frac{q}{4\pi\epsilon_0 Z_1} + \frac{aV_s}{r} - \frac{q}{4\pi\epsilon_0} \frac{a}{Z_1 r} + \frac{q}{4\pi\epsilon_0 Z_1} \sum_{\ell=1}^{\infty} \left[ \left( \frac{r}{Z_1} \right)^\ell - \frac{a^{2\ell+1}}{(Z_1)^{\ell+1}} \right] P_\ell(\cos\theta)$$

but

$$V = \frac{q}{4\pi\epsilon_0 Z_1} + \frac{q}{4\pi\epsilon_0 Z_1} \sum_{\ell=1}^{\infty} \left( \frac{r}{Z_1} \right)^\ell P_\ell(\cos\theta) = \frac{q}{4\pi\epsilon_0 r_1}$$

where  $r_1$  = distance from charge  $q$  to point  $P$ . Then

$$V = \frac{q}{4\pi\epsilon_0 r_1} + \frac{aV_s}{r} - \frac{q}{4\pi\epsilon_0} \sum_{\ell=1}^{\infty} \frac{a^{2\ell+1}}{(Z_1)^{\ell+1}} \frac{P_\ell(\cos\theta)}{r^{(\ell+1)}}.$$

To determine the induced surface charge density, we evaluate the normal derivation at the surface

$$\left. \frac{\partial V}{\partial r} \right|_{r=a} = -\frac{V_s}{a} + \frac{q}{4\pi\epsilon_0} \sum_{\ell=0}^{\infty} (\ell+1) \frac{a^{(\ell-1)}}{Z_1^{(\ell+1)}} P_\ell(\cos\theta)$$

and the induced charge density,  $\sigma$ , is

$$\sigma = -\epsilon_0 \left( \frac{\partial V}{\partial r} \right)_{r=a} = -\frac{q}{4\pi} \sum_{\ell=0}^{\infty} (\ell+1) \frac{a^{(\ell-1)}}{Z_1^{(\ell+1)}} P_\ell(\cos\theta) + \frac{\epsilon_0 V_s}{a}$$

and for setting  $V_s = 0$

$$\sigma = -\frac{q}{4\pi} \sum_{\ell=0}^{\infty} (\ell+1) \left( \frac{a^{\ell-1}}{Z_1^{\ell+1}} \right) P_\ell(\cos\theta).$$

If we now move the point charge to infinity the primary potential becomes

$$V_0 = -\nabla E = -E_0 Z = -E_0 r \cos\theta = -E_0 r P_1(\cos\theta).$$

We effectively have a uniform electric field of magnitude  $E_0$  aligned along the Z-axis. As before, the induced potential due to the presence of the conducting sphere is

$$V_1 = \sum_{\ell=1}^{\infty} b_{\ell} \frac{P_{\ell}(\cos\theta)}{r^{\ell+1}}$$

and applying the same boundary condition at the sphere surface gives

$$V_S = -E_0 a P_1(\cos\theta) + \sum_{\ell=0}^{\infty} b_{\ell} \frac{P_{\ell}(\cos\theta)}{a^{\ell+1}}$$

$$\text{and } b_0 = V_S a$$

$$b_1 = E_0 a^3$$

$$b_{\ell} = 0 \quad \ell > 1$$

therefore,

$$V = -E_0 r P_1(\cos\theta) + \frac{V_S a}{r} + E \frac{a^3}{r^2} P_1(\cos\theta) .$$

In order to determine the charge density, we evaluate the normal derivative at the surface.

$$\left. \frac{\partial V}{\partial r} \right|_{r=a} = -E_0 P_1(\cos\theta) - \frac{V_S}{a} - 2E_0 P_1(\cos\theta)$$

and the surface charge density,  $\sigma$ , is given by

$$\sigma = -\epsilon_0 \nabla V = \epsilon_0 E_0 P_1(\cos\theta) + \frac{\epsilon_0 V_S}{a} + 2\epsilon_0 E_0 P_1(\cos\theta) .$$

Setting  $V_S = 0$

$$\sigma = 3\epsilon_0 E_0 \cos\theta$$

where  $\sigma$  is the surface charged density induced on a conducting sphere in a uniform electric field.

A.2 The Total Induced Charge on a Lune Where a Uniform Electric Field is Perpendicular to the Lunal Center.

The induced surface charge density everywhere on the balloon surface was shown in Appendix A.1 to be

$$\sigma = 3\epsilon_0 E_0 \cos\theta.$$

If the external electric field vector is perpendicular at the center of the lune, the total induced charge on any given surface element of the lune is (see Figure 10)

$$dQ = 3\epsilon_0 E_0 \cos\theta r^2 \sin\beta \, d\alpha d\beta$$

$r$  = radius of the sphere

$r^2 \sin\beta \, d\beta d\alpha$  = area of the surface element.

From geometry,

$$r \cos\theta = a \cos\alpha$$

$$a = r \sin\beta$$

$$\therefore \cos\theta = \cos\alpha \sin\beta.$$

Thus, the total charge on one quarter of a lune is

$$\begin{aligned} \frac{1}{4} Q_T &= \int_{\frac{1}{4} \text{ lune}} dQ = 3\epsilon_0 r^2 E_0 \int_{\beta=0}^{\pi/2} \int_{\alpha=0}^{\pi/4} \sin^2\beta \cos\alpha \, d\alpha d\beta \\ &= 3\epsilon_0 r^2 E_0 (\sin\alpha) \Big|_0^{\pi/4} \left( \frac{\beta}{2} - \frac{\sin^2\beta}{4} \right) \Big|_0^{\pi/2} \\ &= 3\epsilon_0 r^2 E_0 (\sqrt{2}/2) (\pi/4) \end{aligned}$$

$$\therefore Q_T = 3 \sqrt{2}/2 \pi \epsilon_0 r^2 E_0.$$

A.3 Total Induced Charge on a Lune When the Field Vector is Perpendicular  
at an Arbitrary Point

Again referring to Figure 10, the electric field is perpendicular at point  $\alpha'$ ,  $\beta'$ . The induced charge on one quarter of the lunar surface is

$$Q = \int_{\frac{1}{4} \text{ surface}} dQ = 3\epsilon_0 r^2 E_0 \int_0^{\pi/2} \int_0^{\pi/4} \cos(\theta') \sin\beta \, d\alpha d\beta .$$

From Figure 10,

$$\begin{aligned} \cos(\theta') &= \cos(\Delta\alpha) \cos(\pi/2 - \Delta\beta) \\ &= \cos(\Delta\alpha) \sin\Delta\beta \\ &= \cos(\alpha - \alpha') \sin(\beta - \beta') \end{aligned}$$

then

$$\begin{aligned} Q_1 &= 3\epsilon_0 r^2 E_0 \int_0^{\pi/2} \int_0^{\pi/4} \sin\beta \sin(\beta - \beta') \cos(\alpha - \alpha') \, d\alpha d\beta \\ &= 3\epsilon_0 r^2 E_0 \int \int \sin\beta (\sin\beta \cos\beta' - \cos\beta \sin\beta') (\cos\alpha \cos\alpha' + \sin\alpha \sin\alpha') \, d\alpha d\beta \\ &= 3\epsilon_0 r^2 E_0 \left\{ \left[ \left( \frac{\beta}{2} - \frac{\sin 2\beta}{4} \right) \cos\beta' - \frac{1}{2} \sin 2\beta \sin\beta \right]_0^{\pi/2} \left[ \sin\alpha \cos\alpha' - \right. \right. \\ &\quad \left. \left. \cos\alpha \sin\alpha' \right]_0^{\pi/4} \right\} \\ &= 3\epsilon_0 r^2 E_0 \sqrt{2/2} \left( \pi/4 \cos\beta' - \frac{1}{4} \sin\beta' \right) (\cos\alpha' - \sin\alpha') \\ &= 3\epsilon_0 \sqrt{2/2} \pi/4 r^2 E_0 (\cos\beta' - \frac{2}{\pi} \sin\beta') (\cos\alpha' - \sin\alpha') . \end{aligned}$$

Note that  $\Delta\alpha, \Delta\beta$  are different in each of quarter lunes

$$Q_1: \Delta\alpha = \alpha - \alpha', \quad \Delta\beta = \beta - \beta'$$

$$Q_2: \Delta\alpha = \alpha + \alpha', \quad \Delta\beta = \beta - \beta'$$

$$Q_3: \Delta\alpha = \alpha + \alpha', \quad \Delta\beta = \beta + \beta'$$

$$Q_4: \Delta\alpha = \alpha - \alpha', \quad \Delta\beta = \beta + \beta'.$$

Then

$$Q_2 = 3\epsilon_0 \sqrt{2/2} \pi/4 r^2 E_0 (\cos\beta' - 2/\pi \sin\beta') (\cos\alpha' + \sin\alpha')$$

$$Q_3 = 3\epsilon_0 \sqrt{2/2} \pi/4 r^2 E_0 (\cos\beta' + 2/\pi \sin\beta') (\cos\alpha' + \sin\alpha')$$

$$Q_4 = 3\epsilon_0 \sqrt{2/2} \pi/4 r^2 E_0 (\cos\beta' + 2/\pi \sin\beta') (\cos\alpha' - \sin\alpha')$$

and

$$Q_T = Q_1 + Q_2 + Q_3 + Q_4 = 3\epsilon_0 \sqrt{2/2} r^2 E_0 \cos\beta' \cos\alpha' .$$

## APPENDIX B

As shown in the block diagram of Figure 3, the BEFS electronics package consists of four major sections: the electric field sensors and conditioning electronics; the auxiliary data sensors and their associated electronics; the multiplexer and digital conversion section; and the transmitter section. Section 3.5 gave a brief description of the electronics system. This appendix documents the circuits actually used.

B.1 Figure B-1 shows the original electrometer amplified. Current flowing between the sensors is converted by a voltage by the R-C filter. This voltage is then amplified by the instrumentation amplifier. The frequency response of this amplifier is shown in Figure 8.

The diodes protect the front end amplifiers from current spikes caused by large changes in the external electric field. The analog switches provide checks for D.C. offsets. This allows compensation for temperature drifts.

B.2 Charge Amplifier. Figure B-2 is a schematic of the newly designed charge amplifier. The voltage output from this amplifier is directly proportional to the charge flowing between sensors as long as the system is in the linear portion of its response curve. See Figure 8 for the frequency response of this amplifier. The equation for the output from this amplifier is

$$e_o = - \frac{\Delta Q}{C_F}$$

Diodes protect the FET op-amps from transients.

**B.3 Compressor Amplifier.** The schematic for the compressor amp is shown in Figure B-3. This amp effectively increases the dynamic range of the electric field meters. If the signal from the front end amplifier is less than  $\pm 2$  volts, it is amplified by a factor of four. If the signal is greater than  $\pm 2$ , the compressor amp gain factor is one-fourth for that portion of the signal in excess of  $\pm 2$  volts.

**B.4 Auxiliary Data Circuits.** Figure B-4 consists of a number of voltage regulators and auxiliary circuits. The regulator component includes two dual-tracking  $\pm 15$  volt regulators, a  $+5$  volt regulator, and a  $+12.5$  volt regulator. The auxiliary circuits include a precision 200 m-amp constant current source, three high-gain magnetometer amplifiers, an I.C. pressure transducer, and two thermistor circuits.

**B.5 Digital Control Board** as shown in Figure B-5 includes a crystal clock, a 16 channel analog multiplexer, counters, and logic gates. This board controls the data flow from the multiplexer to the sample/hold amplifier and the analog to digital (A/D) converter. This board also contains the logic that converts the parallel two's complement output from the A/D converter into either bi-phase or non-return-to-zero coding.

**B.6 The Digital Conversion Board** (Figure B-6) includes a sample/hold amplifier, 12 bit A/D converter and shift registers. The components on this board convert the analog data into a pulse-code-modulated digital format.

B.7 The Transmitter Board (Figure B-7) consists of a DC-DC converter, regulator, frequency modulator, and a 1680 mhz transmitter. The DC-DC converter increases the battery voltage from 5.6 volts to over 100 volts. This voltage is then regulated to approximately 90 volts and is fed to the plate of the transmitter tube. This plate voltage is modulated via the capacitively coupled PCM data. Modulating the plate voltage causes changes in the transmitter output frequency. In this manner the PCM encoded data frequency modulates the transmitter.

## REFERENCES

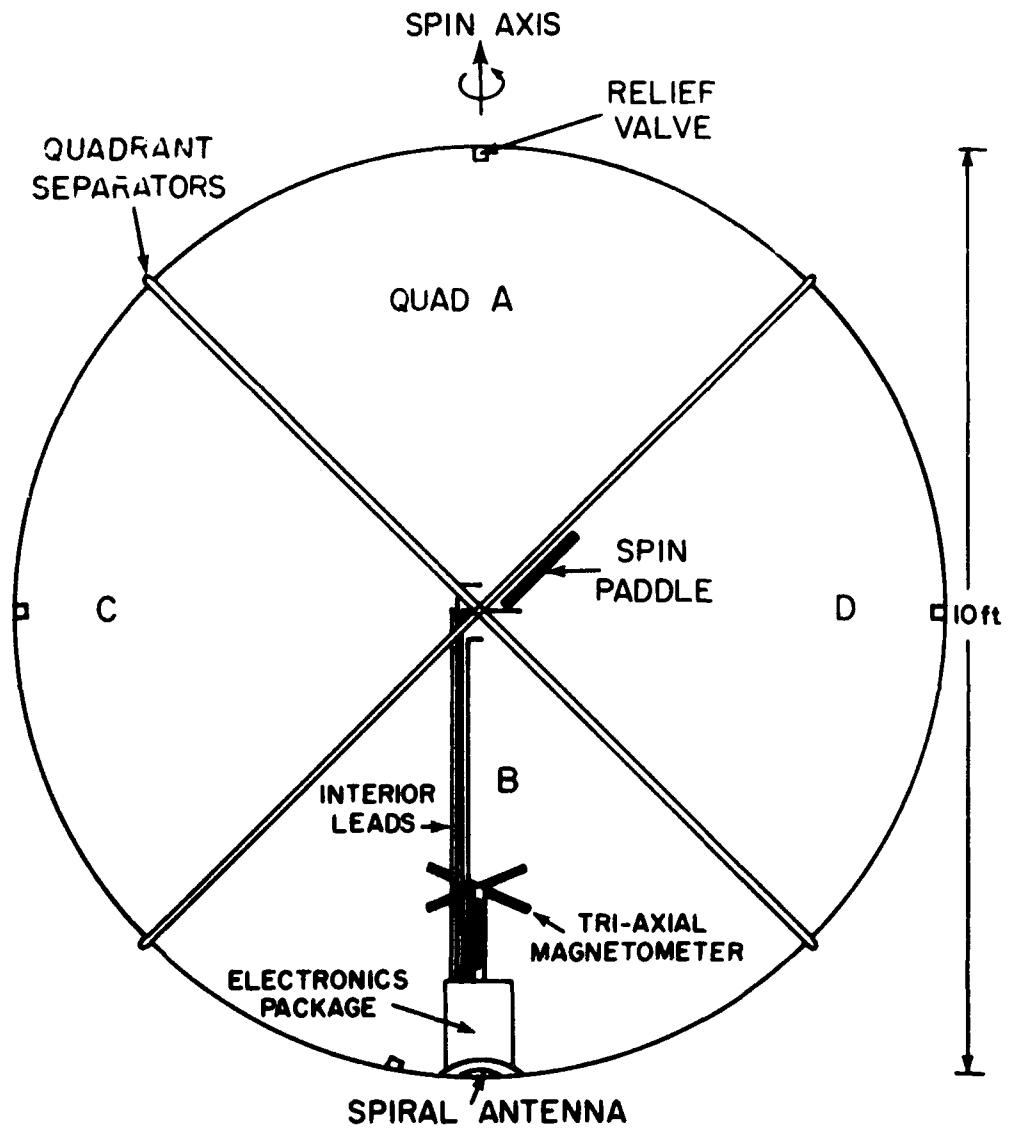
- Chapman, S., Thundercloud electrification in relation to rain and snow particles, Thunderstorm Electricity, Chicago Press, 207, 1953.
- Christian, H.J. and A.A. Few, The measurement of atmospheric electric fields using a newly developed balloon-borne sensor, to be published in the Proceedings of the Fifth International Conference on Atmospheric Electricity, Garmish-Partenkirchen, Germany, 1974.
- Evans, W.H., Electric fields and conductivity in thunderclouds, J. Geophys. Res., 74, 939, 1969.
- Gish, O.H., Evaluation and interpretation of the columnar resistance of the atmosphere, Terr. Magn. Atmos. Elect., 49, 159, 1944.
- Holitzer, F. James, Heinz W. Kasemir, William E. Cobb and W. David Rusk, Aircraft measurements of electric fields in and below thunderstorms, BOS Trans., AGU, 56, 1131, 1974.
- Kasemir, H.W., The cylindrical field mill, Meteorolog. Rundschau, 25, 33, 1972.
- Latham, J. and C.D. Stow, Airborne studies of the electrical properties of large convective clouds, Quart. J. R. Met. Soc., 95, 486, 1969.
- Markson, Ralph, Airborne atmospheric electrical measurements of the variation of ionospheric potential and electrical structure in the exchange layer over the ocean, to be published in the Proceedings of the Fifth International Conference on Atmospheric Electricity, Garmish-Partenkirchen, Germany, 1974.
- Rusk, W.D. and C.B. Moore, Electrical conditions near the base of thunderclouds, over New Mexico, Quart. J. R. Met. Soc., 100, 450, 1974.

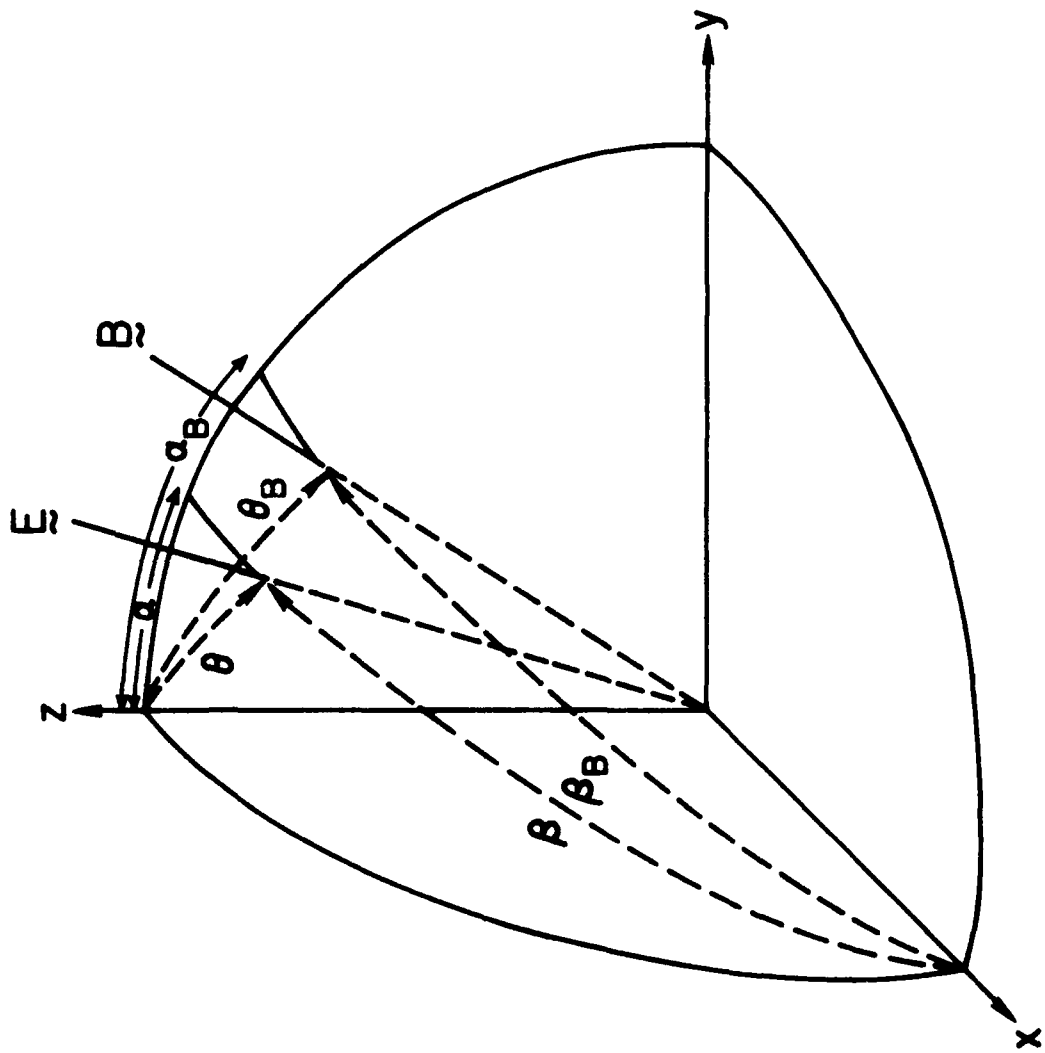
- Simpson, G.C. and F.J. Scarse, The distribution of electricity in thunderclouds, Proc. R. Soc. London, A, 161, 308, 1937.
- Simpson, G.C. and G.D. Robinson, The distribution of electricity in thunderstorms, II, Proc. R. Soc. London, A, 177, 201, 1940.
- Stratton, J.A., Electromagnetic Theory, McGraw-Hill, New York, 1941.
- Wilson, C.R.T., A theory of thunderstorm electricity, Proc. Roy. Soc., (A), 236, 297, 1956.
- Winn, W.P. and L.G. Byerley, Electric field growth in thunderclouds, to be published in Quart. J. R. Met. Soc., 1975.
- Winn, W.P. and C.B. Moore, Electric field measurements in thunderclouds using instrumented rockets, J. Geophys. Res., 76, 5003, 1971.
- Winn, W.P., Schwede, G.W. and C.B. Moore, Measurements of electric fields in thunderclouds, J. Geophys. Res., 79, 1761, 1974.

## FIGURE CAPTIONS

- Figure 1** Physical configuration of the Balloon Electric Field Sensor.
- Figure 2** Balloon coordinate system. Direction cosines to B and E are indicated.
- Figure 3** Block diagram of the Balloon Electric Field Sensor data acquisition system.
- Figure 4** Picture of launch from Palestine, Texas.
- Figure 5** Altitude, pressure and temperature profiles vs. time into flight. Corrective altitude/pressure and temperature data are from rawinsonde measurements. The rawinsonde was launched from Shreveport, Louisiana at 20:22 EDT on 17 May 1974.
- Figure 6** Electric field measurements at two periods during the flight using the derivative model calculations. The top dashed line was plotted using an empirical equation that models the fair weather electric field (Gish, 1944). The bottom dashed line was

- plotted from fair weather field measurements made by Fitzgerald.
- Figure 7** Electric field measurements made during the test flight. Calculations were made using the integration model. Figures 6 and 7 are drawn to the same scale.
- Figure 8** Amplifier frequency response curves. Shows the comparative response characteristics of the original voltage amplifier and the newer charge amplifier.
- Figure 9** Conducting sphere near a point charge.
- Figure 10** Geometry of the lunar surface.
- Figure B-1** Electrometer amplifier schematic.
- Figure B-2** Charge amplifier schematic.
- Figure B-3** Compressor amplifier schematic.
- Figure B-4** Schematics of the auxiliary data circuits.
- Figure B-5** Digital control board schematic.
- Figure B-6** Digital conversion board schematic.
- Figure B-7** Transmitter board schematic.





# BEFS BLOCK DIAGRAM

